Magnetic field amplification during the common envelope phase

Sebastian T. Ohlmann,[1,2]★ Friedrich K. Röpke,[1,3] Rüdiger Pakmor,[1] Volker Springel[1,4] and Ewald Müller[5]

[1]*Heidelberger Institut für Theoretische Studien, Schloss-Wolfsbrunnenweg 35, D-69118 Heidelberg, Germany*
[2]*Institut für Theoretische Physik und Astrophysik, Universität Würzburg, Emil-Fischer-Str. 31, D-97074 Würzburg, Germany*
[3]*Zentrum für Astronomie der Universität Heidelberg, Institut für Theoretische Astrophysik, Philosophenweg 12, D-69120 Heidelberg, Germany*
[4]*Zentrum für Astronomie der Universität Heidelberg, Astronomisches Recheninstitut, Mönchhofstr. 12-14, D-69120 Heidelberg, Germany*
[5]*Max-Planck-Institut für Astrophysik, Karl-Schwarzschild-Str. 1, D-85748 Garching, Germany*

ABSTRACT

During the common envelope (CE) phase, a giant star in a binary system overflows its Roche lobe and unstable mass transfer leads to a spiral-in of the companion, resulting in a close binary system or in a merger of the stellar cores. Dynamo processes during the CE phase have been proposed as a mechanism to generate magnetic fields that are important for forming magnetic white dwarfs (MWDs) and for shaping planetary nebulae. Here, we present the first magnetohydrodynamics simulations of the dynamical spiral-in during a CE phase. We find that magnetic fields are strongly amplified in the accretion stream around the 1 $M_\odot$ companion as it spirals into the envelope of a 2 $M_\odot$ RG. This leads to field strengths of 10–100 kG throughout the envelope after 120 d. The magnetic field amplification is consistent with being driven by the magnetorotational instability. The field strengths reached in our simulation make the magnetic field interesting for diagnostic purposes, but they are dynamically irrelevant. They are also too small to explain the formation of the highest fields found in MWDs, but may be relevant for luminous red novae, and detecting magnetic fields in these events would support the scenario as proposed here.

Key words: hydrodynamics – magnetic fields – MHD – methods: numerical – binaries: close – white dwarfs.

1 INTRODUCTION

The CE phase is usually invoked to explain the formation of close binary systems with at least one compact star: the compact star is born as a core of a giant with a much larger radius than the separation of the observed binary. During the CE phase, angular momentum and energy is extracted from the system as the envelope is ejected and a close binary system emerges. Results of this evolution include cataclysmic variables (CVs; King 1988; Ritter & Kolb 2003), close WD and main-sequence (MS) binaries (Schreiber & Gänsicke 2003; Zorotovic et al. 2010), double WDs (Iben & Tutukov 1985; Han, Podsiadlowski & Eggleton 1995; Nelemans et al. 2001), Type Ia supernovae (Iben & Tutukov 1984; Ruiter, Belczynski & Fryer 2009; Toonen, Nelemans & Portegies Zwart 2012), and many more (see also the reviews by Iben & Livio 1993; Taam & Sandquist 2000; Ivanova et al. 2013a).

The origin of magnetic fields in stars is still unknown, and it is debated if they are remainders from fields generated during the formation of a star (fossil field hypothesis) or if they are generated during the life of a star by dynamo processes (Ferrario, Melatos & Zrake 2015a). WDs show magnetic fields with strengths up to 10^9 G and can also occur in binaries with accretion from a low-mass companion, so-called magnetic CVs (Ferrario, de Martino & Gänsicke 2015b). The absence of magnetic WDs in wide binaries suggests a binary origin for both magnetic WDs and magnetic CVs (Tout et al. 2008; Briggs et al. 2015). In this scenario, magnetic fields are amplified by a dynamo process in the differentially rotating envelope during a CE phase (Regős & Tout 1995) or in an accretion disc around the giant core that was formed from the tidally disrupted companion (Nordhaus et al. 2011). The magnetic fields created during the CE phase have to be much larger than the final surface field of the WD because it is difficult to anchor the fields on the WD (Potter & Tout 2010). At the high-mass end of magnetic WDs, mergers of two WDs constitute a different channel that can explain large magnetic fields (Zhu et al. 2015). In their population study, Briggs et al. (2015) find that the major contribution comes from mergers during the CE phase.

Magnetic fields generated during the CE phase may also affect the shape and evolution of planetary nebulae (PNe) (Nordhaus & Blackman 2006; Nordhaus, Blackman & Frank 2007). The magnetic field generation relies again on a dynamo process in

★ E-mail: sebastian.ohlmann@h-its.org

the differentially rotating envelope or in an accretion disc formed by the tidally disrupted companion. Magnetic fields have not been detected in post-AGB stars as remnants of PNe; the upper limits lie at 100–300 G (Jordan et al. 2012). Tocknell, De Marco & Wardle (2014) used observational data on four jets in PNe to constrain the magnetic fields that are necessary to launch these jets via the Blandford–Payne mechanism (Blandford & Payne 1982) to hundreds of G to a few kG. Three jets pre-date the CE event by few thousand years, one jet post-dates the CE event by a few thousand years. Thus, besides binarity itself (De Marco 2009), magnetic fields can be an important factor for shaping PNe.

Up to now, the generation of magnetic fields during the CE phase was attributed to dynamo processes driven by shear due to differential rotation in the envelope or in an accretion disc. Here, we present the first magnetohydrodynamics simulations of the dynamical spiral-in during a CE phase. The simulations extend the hydrodynamics simulation of a CE phase of a 2 $M_\odot$ RG interacting with a 1 $M_\odot$ companion presented by Ohlmann et al. (2016) and account for MHD effects.

2 METHODS

The magnetohydrodynamics simulations presented here employ the moving-mesh code AREPO (Springel 2010) with additional modifications as introduced in Pakmor et al. (2016) and Ohlmann et al. (2016). As initial model, the same 1.98 $M_\odot$ RG with a 0.4 $M_\odot$ He core is used as by Ohlmann et al. (2016) after a relaxation step, during which spurious velocities are damped to reach a stable equilibrium. The core of the RG and the companion (1 $M_\odot$) are represented by point masses with a gravitational potential that is softened at a length $h \approx 2.8$ $R_\odot$.[1] Around the point masses, an adaptive refinement is enforced with the effective cell radius being smaller than $h/10$ in a sphere of radius $4h$ around each point mass. During the simulation, h is always enforced to be lower than a fifth of the orbital separation. In the rest of the domain, refinement ensures similar cell masses according to the desired resolution. As in Ohlmann et al. (2016), the companion is initially placed at the surface of the RG.

In addition to the simulation presented by (Ohlmann et al. 2016), magnetic fields are included. To this end, the ideal MHD solver as implemented by Pakmor, Bauer & Springel (2011) and improved by Pakmor & Springel (2013) is utilized. As initial conditions, a magnetic dipole field was set up along the z-axis as

$$\boldsymbol{B}(\boldsymbol{r}) = \frac{B_{s,i}}{2} \frac{3\boldsymbol{n}n_z - \boldsymbol{e}_z}{(r/R)^3}, \tag{1}$$

where $B_{s,i}$ denotes the initial surface field strength at the pole, R the stellar radius, $\boldsymbol{r}$ the position inside the star, $\boldsymbol{n} = \boldsymbol{r}/r$ the normalized position, and $\boldsymbol{e}_z$ the unit vector in z direction. The initial surface field is varied in different simulations (see Table 1); a value of 10^{-6} G at the surface of the RG would correspond to a mG surface field at the ZAMS under the assumption of flux freezing. The initial magnetic field energy is negligible compared to the internal energy for all models.

[1] This corresponds to an 'equivalent' Plummer softening length $\epsilon \approx 1$ $R_\odot$ (the value that was quoted in Ohlmann et al. 2016), see also the discussion of equation (108) in Springel (2010).

Table 1. Simulation properties.

$B_{s,i}$[a] (G)	Cells (10^6)	t_{amp}[b] (d)	$\langle E_B \rangle$[c] (10^{44} erg)	a_f[d] ($R_\odot$)	m_{ej}/m_{env}[e]
10^{-6}	2.6	3.5	3.9	4.30	6.5 per cent
10^{-6}	7.7	2.9	4.1	4.42	6.2 per cent
10^{-2}	2.6	3.3	4.5	4.33	6.3 per cent
10^{-10}	2.6	3.1	5.0	4.39	6.2 per cent
0[f]	2.7	–	–	4.22	5.2 per cent

Notes. [a]Initial magnetic field strength at the stellar surface.
[b]Amplification time-scale fitted to the increase in the magnetic energy between 3 and 20 d.
[c]Mean magnetic field energy between 25 and 140 d.
[d]Final semi-major axis at 120 d.
[e]Unbound mass over envelope mass.
[f]Non-MHD simulation from Ohlmann et al. (2016).

3 RESULTS

3.1 Overall evolution

The magnetic fields during the evolution are strongly amplified with a similar evolution of the magnetic energy for all simulations (Table 1, Fig. 1) and is thus independent of the choice of the initial surface field strength. The evolution of the magnetic fields can be subdivided into three phases: an initial, fast amplification phase up to 3 d (lasting less than a fifth of the first orbit; Fig. 1, panel c), a slow amplification phase between 3 and 20 d (ending after slightly more than the first orbit; Fig. 1, panel d), and a saturation phase after 20 d (Fig. 1, panel b). During the fast amplification phase, an accretion stream around the companion emerges (shown in Fig. 2 at 1.5 d), and the magnetic field is amplified in this stream with an e-folding time of roughly 0.1 d (cf. Fig. 1, panel c). Regardless of the initial surface magnetic field (10^{-10}, 10^{-6}, and 10^{-2} G, see Table 1), the total magnetic energy reaches a similar value of 2–3 $\times 10^{42}$ erg after this phase at 3 d (Fig. 1, panel c); the further evolution is very similar for the different simulations (see panels d and b). For the highest surface field (10^{-2} G, red dotted line in Fig. 1), the total magnetic energy is initially dominated by the initial field configuration in the RG, which is unstable and decays; after 1 d, the total magnetic energy is already dominated by the fields around the companion (Fig. 1, panel c). During the slow amplification phase, the accretion stream is established and the amplification time-scale decreases to about 3 d (see Table 1; Fig. 1, panel d; Fig. 2 at 8 d). After 20 d and slightly more than one orbit, the system enters the saturation phase and the total magnetic energy remains more or less constant at 4–5 $\times 10^{44}$ erg (Fig. 1, panel b; Fig. 2 at 20 d and at 120 d; Table 1), which is less than a per cent of the total energy of the system (-2.3×10^{47} erg).

As a check, the simulation with $B_{s,i} = 10^{-6}$ G was repeated with a finer mass resolution of 7.7 million cells as opposed to 2.6 million cells for the other runs; this increase by a factor of 3 corresponds on average to an increase in spatial resolution by a factor of about 1.4. The evolution of this simulation is very similar to the lower resolution simulation: the separation does not change significantly and the total magnetic energy deviates only between 15 and 40 d, when it is slightly larger for the high-resolution run (Fig. 1). As demonstrated by Ohlmann et al. (2016), it is important to resolve the gravitational interaction between the point masses and the gas which is ensured by requiring an effective resolution of at least 10 cells per softening length already in the lower resolution simulation. Increasing the resolution in the rest of the envelope does
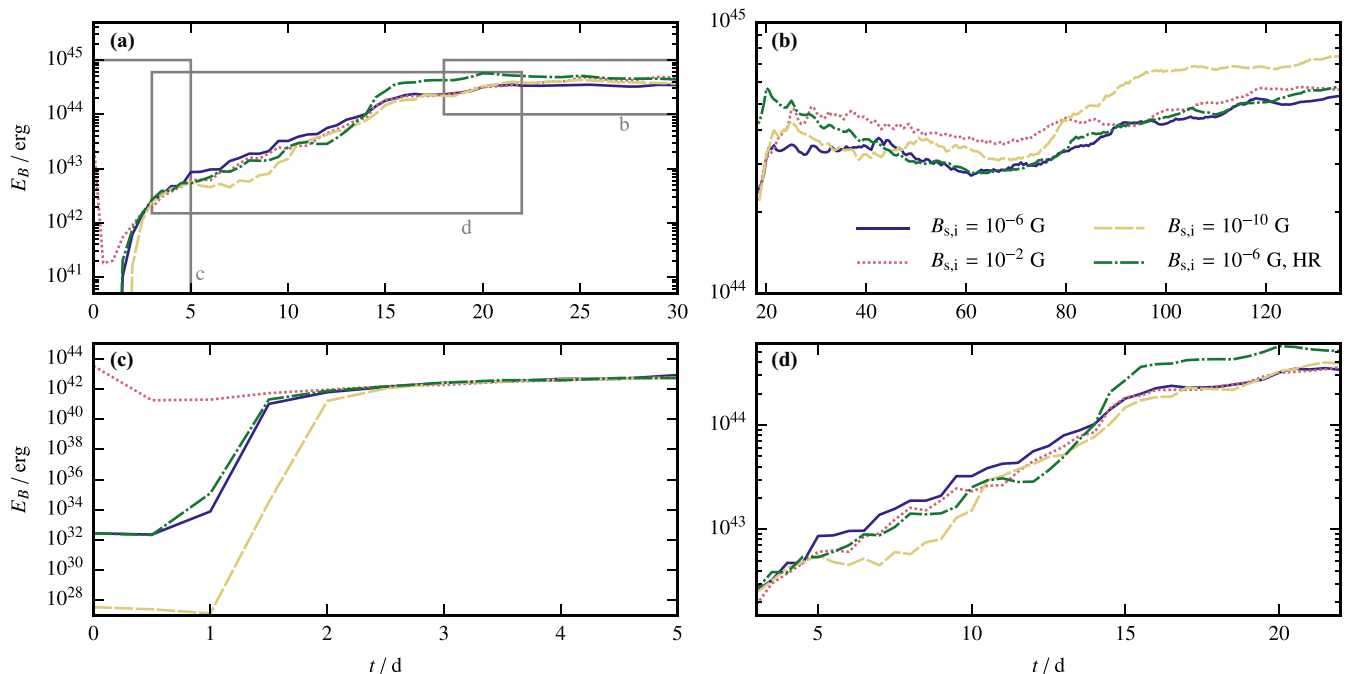
Figure 1. Magnetic field energy over time for different simulations. Panel (a) displays the evolution until 30 d, panel (b) zooms in on the saturation phase during which the magnetic field energy stays nearly constant. Panel (c) shows the fast amplification phase during the first 5 d of the simulations. In panel (d), the slow amplification phase is shown, which is very similar for all simulations. The simulations started with a different initial surface field $B_{s,i}$. HR denotes the high-resolution simulation.

not significantly change the outcome. Moreover, an additional check with reduced resolution around the cores (five cells per softening length) does not change the outcome significantly, either. Hence, the most important processes seem to be resolved by imposing the adaptive refinement around the cores to at least 5–10 cells per softening length.

Compared to the non-MHD run by Ohlmann et al. (2016), the evolution of the orbit is very similar with the final separation at 120 d being at most 5 per cent larger for the MHD simulations (Table 1). Thus, the dynamical impact of the magnetic fields is small, although slightly more mass is unbound during the first orbit (between 6.2 per cent and 6.5 per cent of the total envelope mass compared to 5.2 per cent without magnetic fields after 60 d), but the difference becomes smaller at later times, when the ejected mass increases. Moreover, the components of the magnetic stress tensor are small compared to those of the hydrodynamic stress tensor, and the contribution of magnetic fields to angular momentum transport is small at all times.

The time evolution of the magnetic field structure is shown in Fig. 2 in the orbital plane (upper row) and perpendicular to it (lower row), centred on the companion. During the amplification phases, up to 20 d, the magnetic field strength increases in the accretion stream around the companion and the region of very strong magnetic fields (larger than 1/10 of the maximum field strength) is confined to about 2 $R_\odot$ around the companion. At the end of the slow amplification phase (Fig. 2 at 20 d), the magnetic fields start to be advected through the envelope. At later times (Fig. 2 at 120 d), the magnetic field is dispersed throughout the envelope, reaching values of 10–100 kG in large parts of the envelope.

3.2 Comparison to MRI

The flow structure around the companion resembles an accretion flow with radially decreasing angular velocity Ω. In the presence of magnetic fields, such a configuration is unstable and subject to the magnetorotational instability (MRI; Balbus & Hawley 1991; Balbus 1995; for a review see Balbus & Hawley 1998). During the linear phase, this instability leads to exponentially growing magnetic fields, finally ending in a saturated state due to non-linear interactions. The *e*-folding time during the growth phase is usually dominated by the fastest growing MRI channel (e.g. Rembiasz et al. 2016); its growth time is given by (Rembiasz et al. 2016, equation 25)

$$t_{mri} = \frac{2}{q}\frac{1}{\Omega}, \tag{2}$$

and the associated wavenumber can be computed as (Rembiasz et al. 2016, equation 24)

$$k_{mri} = \sqrt{1 - \frac{2-q^2}{4}}\frac{\Omega}{v_{Az}}, \tag{3}$$

where $q = -\mathrm{d}\ln\Omega/\mathrm{d}\ln r$ is the local rotational shear and $v_{Az} = B_z/\sqrt{4\pi\rho}$ the Alfvén velocity in z direction. The wavelength of the corresponding MRI channel is $\lambda_{mri} = 2\pi/k_{mri}$. In the simulations, q takes values of about 1, thus the flow is unstable to the MRI. The mean value of Ω around the companion rises to 4.4×10^{-4} s^{-1} during the first 0.5 d and then slowly declines to 5.7×10^{-5} s^{-1} at 25 d. The Alfvén velocity increases quickly at the beginning as the magnetic field is advected towards the companion and then further as the MRI operates. It reaches a maximum of 1.3×10^6 cm s^{-1} at 5 d.

In the simulations, the amplification of the magnetic fields starts when the fastest growing mode is resolved on the grid after 0.5–1 d, with the smallest grid cells having an effective radius of approximately 0.02 $R_\odot$. The *e*-folding time of the magnetic energy during the fast amplification phase between 0.5 and 2 d (Fig. 1, panel c) is about 0.05 d, which is similar to the time-scale of the fastest
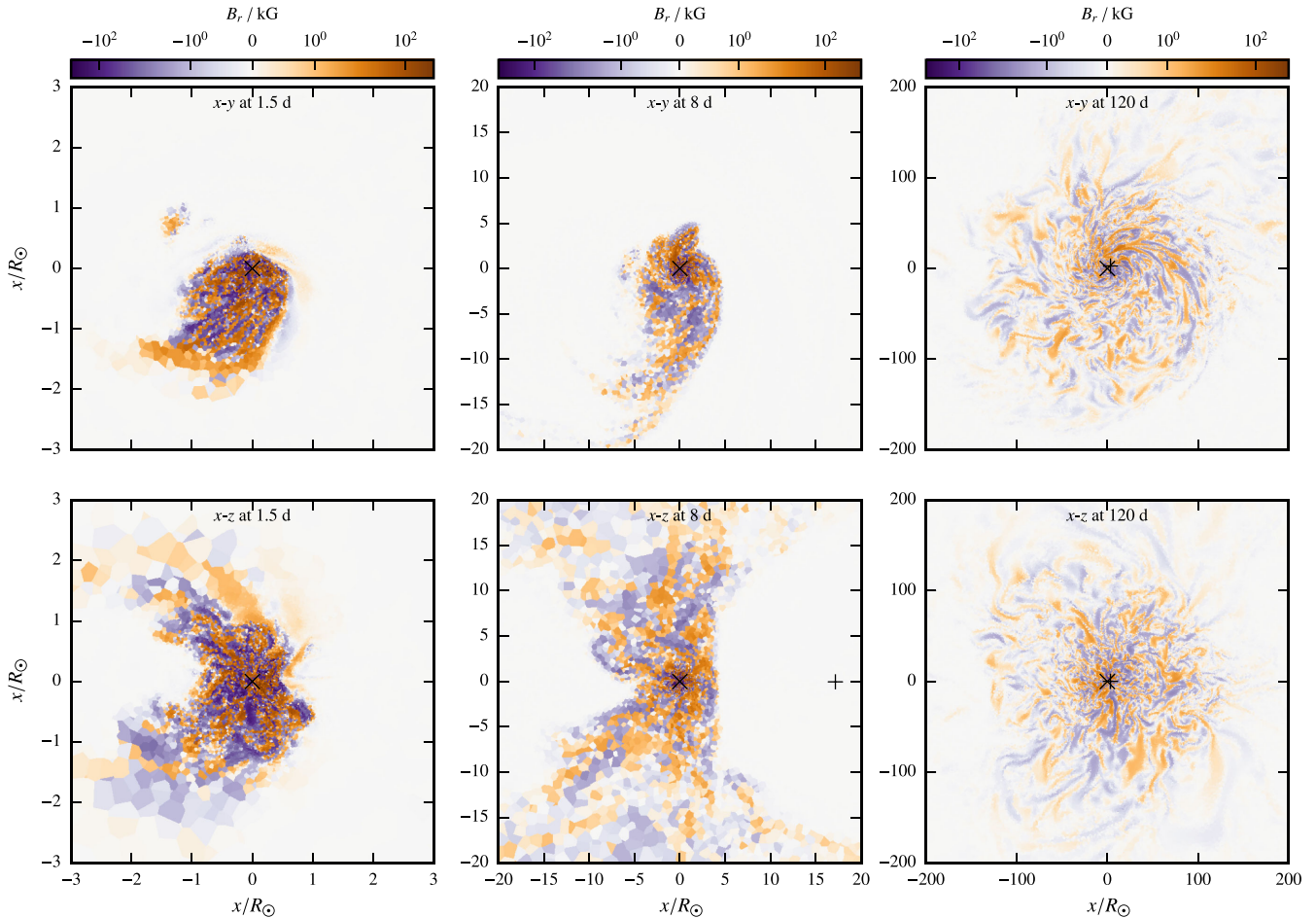
Figure 2. Magnetic field configuration over time for the high-resolution simulation with $B_{s,\,i} = 10^{-6}$ G. Displayed is the radial magnetic field B_r in the x–y plane (upper row) and in the x–z plane (lower row) at three different times in an increasingly larger area centred on the companion. The position of the companion is marked by a ×, the position of the RG core is marked by a +; in the x–z plane, the position of the RG core is projected on to the plane. The RG core is located outside of the region shown in the two leftmost columns. The colour scale is linear between −10 and 10 kG and logarithmic for positive and negative values outside of this range.

growing MRI channel (between 0.05 and 0.2 d) as estimated as a mean value from the simulation using equation (2). Since the flow structure in the simulation is not an idealized shearing box, no pure MRI channels are expected to emerge and estimates using the formulae above are only approximate.

During the evolution, the size of the fastest growing MRI channel increases due to an increase of the Alfvén velocity and at 1.5 d, it becomes larger than the accretion flow structure, which has a radius of about 2 $R_\odot$.[2] Thus, the MRI can only operate on smaller wavelengths and longer growth times: the e-folding time of the magnetic energy during the slow amplification phase is about 3 d (see Table 1 and Fig. 1, panel d), but the fastest MRI time-scale t_{mri} at this point is about 1 d. It has increased because the angular velocity has decreased (cf. equation 2).

After 20 d, the growth of the magnetic energy stops and the system transitions to a saturation phase (Fig. 1, panel b). This may be attributed to a change in the flow structure: the accretion flow around the companion is disturbed by the interaction with the RG

core because the separation is only 10 $R_\odot$ at periapsis at this time. Possible reasons usually invoked for termination of the MRI include parasitic instabilities (Goodman & Xu 1994). Moreover, it is unclear what determines the level at which the magnetic fields saturate; this may depend on the system parameters such as the evolutionary state (e.g. RGB or AGB) or mass of the primary or the initial configuration of the system. As an additional test, we conducted a simulation with a smaller companion mass (0.5 $M_\odot$), but otherwise identical initial conditions. In this run, the same saturation level of the magnetic energy is reached as for the 1 $M_\odot$ companion, thus other factors are more important than the companion mass.

4 DISCUSSION

The first MHD simulations of the CE phase show that magnetic fields are strongly amplified in the direct vicinity of the companion star on dynamical time-scales during the spiral-in. The temporal and spatial scales are compatible with the MRI operating in the accretion flow around the companion. Although the magnetic field strength is increased by orders of magnitude, the dynamical impact is small: mass loss is slightly increased during the first orbit (about 5–6 per cent), but the contribution to angular momentum and energy

---

[2] The magnetic field down to a tenth of the maximum field strength is also confined to this region during the first 20 d.

transport is not significant and the final separation of the stellar cores is very similar to that found in non-MHD simulations with the same initial parameters.

This is a new way of generating magnetic fields during the dynamical spiral-in of the CE phase compared to earlier investigations that assumed a dynamo operating in the differentially rotating envelope (Regős & Tout 1995), in an accretion disc formed from the tidally disrupted companion (Nordhaus et al. 2011), or in the hot outer layers of the degenerate core (Wickramasinghe, Tout & Ferrario 2014). These processes, however, may still be important later in the evolution. We also stress that we only simulated a single system, and that a variety of systems undergoing a CE phase has to be simulated to understand the range of magnetic fields that can be generated during CE evolution.

Magnetic fields that vary on short time-scales, as is the case in the simulations presented here, are difficult to anchor at the WD surface (Potter & Tout 2010). Moreover, the magnetic fields present in the simulations (10–100 kG) are smaller than the largest fields in WDs (up to 10^9 G, see Ferrario et al. 2015b). Thus, the dynamical amplification of magnetic fields during the spiral-in may not explain the formation of high-field magnetic WDs for the simulated CE phase of a 2 M$_\odot$ RG. According to the population synthesis calculations by Briggs et al. (2015), the largest contribution to high-field magnetic WDs comes from mergers during the CE phase of an AGB primary. Hence, such systems may be more promising for future studies.

RGs can be observed with mean magnetic fields down to 10–100 G, but all observed RGs with magnetic fields cluster at the base of the RG branch (Aurière et al. 2015). Because it is difficult to compute the photosphere in our simulations, the magnetic field at the photosphere cannot be predicted from our simulations, and we postpone such an analysis to future studies. Nevertheless, CE events have been connected to luminous red novae (LRN; Ivanova et al. 2013b), and the presence of magnetic fields in these events would support dynamical amplification during the spiral-in phase of a CE event.

REFERENCES

Aurière M. et al., 2015, A&A, 574, A90
Balbus S. A., 1995, ApJ, 453, 380
Balbus S. A., Hawley J. F., 1991, ApJ, 376, 214
Balbus S. A., Hawley J. F., 1998, Rev. Mod. Phys., 70, 1
Blandford R. D., Payne D. G., 1982, MNRAS, 199, 883
Briggs G. P., Ferrario L., Tout C. A., Wickramasinghe D. T., Hurley J. R., 2015, MNRAS, 447, 1713
De Marco O., 2009, PASP, 121, 316
Ferrario L., Melatos A., Zrake J., 2015a, Space Sci. Rev., 191, 77
Ferrario L., de Martino D., Gänsicke B. T., 2015b, Space Sci. Rev., 191, 111
Goodman J., Xu G., 1994, ApJ, 432, 213
Han Z., Podsiadlowski P., Eggleton P. P., 1995, MNRAS, 272, 800
Iben I., Jr, Livio M., 1993, PASP, 105, 1373
Iben I., Jr, Tutukov A. V., 1984, ApJS, 54, 335
Iben I., Jr, Tutukov A. V., 1985, ApJS, 58, 661
Ivanova N. et al., 2013a, A&AR, 21, 59
Ivanova N., Justham S., Nandez J. L. A., Lombardi J. C., 2013b, Science, 339, 433
Jordan S., Bagnulo S., Werner K., O'Toole S. J., 2012, A&A, 542, A64
King A. R., 1988, QJRAS, 29, 1
Nelemans G., Yungelson L. R., Portegies Zwart S. F., Verbunt F., 2001, A&A, 365, 491
Nordhaus J., Blackman E. G., 2006, MNRAS, 370, 2004
Nordhaus J., Blackman E. G., Frank A., 2007, MNRAS, 376, 599
Nordhaus J., Wellons S., Spiegel D. S., Metzger B. D., Blackman E. G., 2011, Proc. Natl. Acad. Sci., 108, 3135
Ohlmann S. T., Röpke F. K., Pakmor R., Springel V., 2016, ApJ, 816, L9
Pakmor R., Springel V., 2013, MNRAS, 432, 176
Pakmor R., Bauer A., Springel V., 2011, MNRAS, 418, 1392
Pakmor R., Springel V., Bauer A., Mocz P., Munoz D. J., Ohlmann S. T., Schaal K., Zhu C., 2016, MNRAS, 455, 1134
Potter A. T., Tout C. A., 2010, MNRAS, 402, 1072
Regős E., Tout C. A., 1995, MNRAS, 273, 146
Rembiasz T., Obergaulinger M., Cerdá-Durán P., Müller E., Aloy M. A., 2016, MNRAS, 456, 3782
Ritter H., Kolb U., 2003, A&A, 404, 301
Ruiter A. J., Belczynski K., Fryer C., 2009, ApJ, 699, 2026
Schreiber M. R., Gänsicke B. T., 2003, A&A, 406, 305
Springel V., 2010, MNRAS, 401, 791
Taam R. E., Sandquist E. L., 2000, ARA&A, 38, 113
Tocknell J., De Marco O., Wardle M., 2014, MNRAS, 439, 2014
Toonen S., Nelemans G., Portegies Zwart S., 2012, A&A, 546, A70
Tout C. A., Wickramasinghe D. T., Liebert J., Ferrario L., Pringle J. E., 2008, MNRAS, 387, 897
Wickramasinghe D. T., Tout C. A., Ferrario L., 2014, MNRAS, 437, 675
Zhu C., Pakmor R., van Kerkwijk M. H., Chang P., 2015, ApJ, 806, L1
Zorotovic M., Schreiber M. R., Gänsicke B. T., Nebot Gómez-Morán A., 2010, A&A, 520, A86

This paper has been typeset from a TEX/LATEX file prepared by the author.